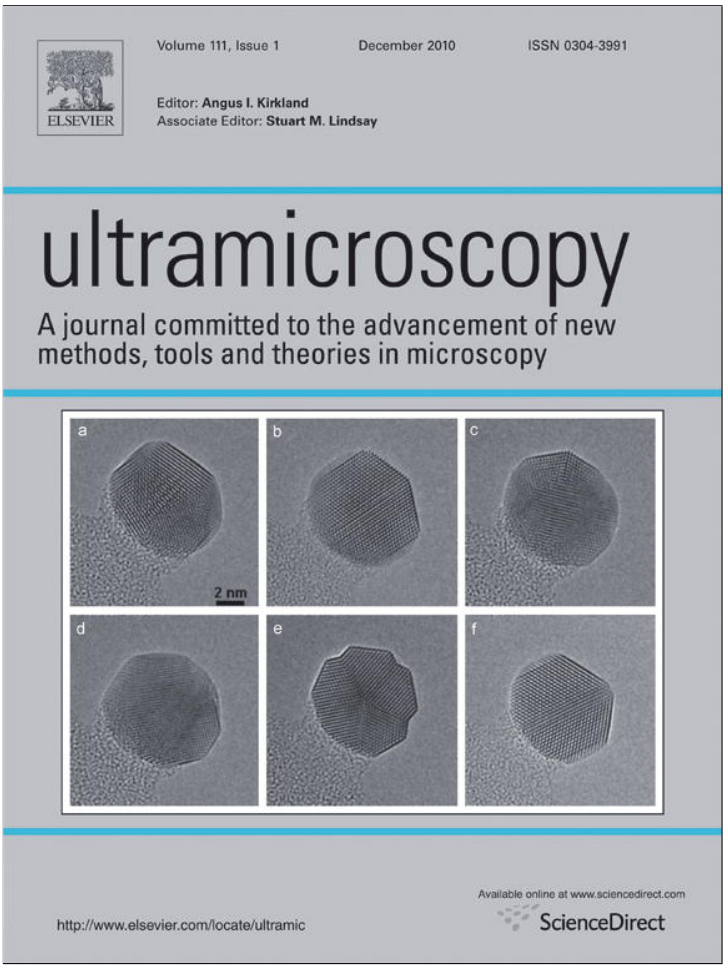

Ultramicroscopy 111 (2010) 11–19

Contents lists available at ScienceDirect

Ultramicroscopy

journal homepage: www.elsevier.com/locate/ultramic

A force-matching method for quantitative hardness measurements by atomic force microscopy with diamond-tipped sapphire cantilevers

Frederic Sansoz [a,b,*], Travis Gang [a]

[a] School of Engineering, University of Vermont, Burlington, VT 05405, USA
[b] Materials Science program, University of Vermont, Burlington, VT 05405, USA

ARTICLE INFO

Article history:
Received 24 March 2010
Received in revised form
28 July 2010
Accepted 29 September 2010

Keywords:
Atomic force microscopy nanoindentation
Diamond tip
Force calibration
Hardness measurements
Finite element analysis

ABSTRACT

We present a new method to improve the accuracy of force application and hardness measurements in hard surfaces by using low-force (<50 μN) nanoindentation technique with a cube-corner diamond tip mounted on an atomic force microscopy (AFM) sapphire cantilever. A force calibration procedure based on the force-matching method, which explicitly includes the tip geometry and the tip-substrate deformation during calibration, is proposed. A computer algorithm to automate this calibration procedure is also made available. The proposed methodology is verified experimentally by conducting AFM nanoindentations on fused quartz, Si(1 0 0) and a 100-nm-thick film of gold deposited on Si(1 0 0). Comparison of experimental results with finite element simulations and literature data yields excellent agreement. In particular, hardness measurements using AFM nanoindentation in fused quartz show a systematic error less than 2% when applying the force-matching method, as opposed to 37% with the standard protocol. Furthermore, the residual impressions left in the different substrates are examined in detail using non-contact AFM imaging with the same diamond probe. The uncertainty of method to measure the projected area of contact at maximum force due to elastic recovery effects is also discussed.

1. Introduction

Pyramidal diamond tips mounted on atomic force microscopy (AFM) cantilever beams have been used over the past 15 years to perform nanoscale indentations and hardness measurements in ceramics and metals [1–11], as well as in high-modulus polymeric substrates [11–14]. Specialty tips are generally designed for nanoindentation from a natural single-crystal diamond in order to reduce deformation and wear of the tip during contact. In particular, a new combination of diamond tip and sapphire AFM cantilever holds great promise, primarily because sapphire has high mechanical-strength that allows attachment of a massive probe, and facilitates its bonding to the cantilever beam by metal deposition at high temperature [15]. In addition to bulk materials and films, such diamond-tipped AFM cantilevers may advance the mechanical characterization of low-dimensional nanostructures. While a few attempts have been made to indent nanowires using traditional depth-sensing instrumented indentation methods [16–19], AFM nanoindentation has two major advantages for property characterization in nanomaterials. First, non-contact high-resolution imaging of surface areas in AFM nanoindentation provides accurate tip positioning prior to indentation, along with a rapid account of permanent deformations after testing [20–23]. Second, this technique can be readily exploited to perform multi-physical measurements with tools that have already been integrated to recent AFM systems, such as piezoresponse force microscopy [24]. On the other hand, AFM nanoindentation requires complex force calibration procedure for which knowledge of quantities such as cantilever spring constant, the photodetector voltage/height sensitivity and the probe geometry is necessary when transforming raw data into force–displacement nanoindentation curves [25].

Traditionally, the indentation hardness H is estimated from

$$H = \frac{F_{\max}}{A_c}, \tag{1}$$

where $F_{\max}$ is the maximum force applied by a penetrating tip, and A_c is the projected area of contact. Note that in the classic definition, the hardness is based on the contact area measured from the area of the residual impression, which may deviate from that used in depth-sensing nanoindentation technique based on the contact area under load, particularly for very shallow nanoindentations (<50 nm in depth) due to elastic recovery effects [27]. Fig. 1 shows a simplified representation of the process of indentation with a pyramidal tip mounted on an AFM cantilever. The applied force F is controlled through the change in the photodetector voltage *Vpd* due to the cantilever deflection *Zc* in the

* Corresponding author at: School of Engineering, University of Vermont, Burlington, VT 05405, USA. Tel.: +1 802 656 3837; fax: +1 802 656 3358.
E-mail address: frederic.sansoz@uvm.edu (F. Sansoz).

0304-3991/$ - see front matter © 2010 Elsevier B.V. All rights reserved.
doi:10.1016/j.ultramic.2010.09.012

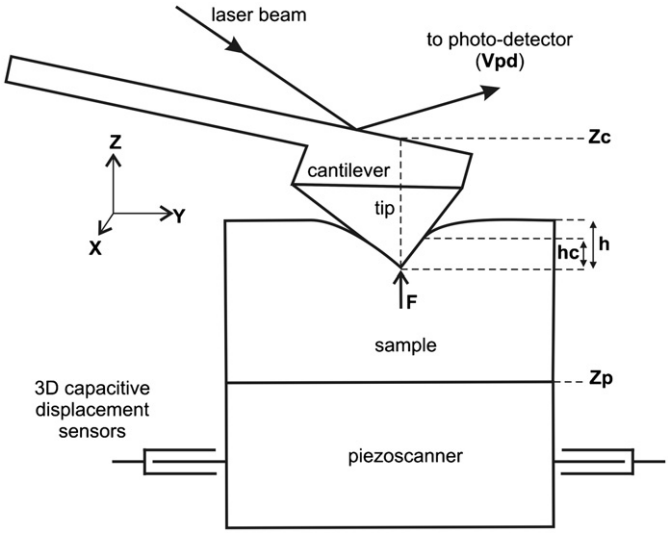

Fig. 1. Simplified representation of the AFM nanoindentation experiment with a cube-corner diamond tip mounted on an AFM cantilever beam.

vertical alignment with the force, as shown in this figure, such that

$$F = k \times Zc, \tag{2}$$

where k represents the normal spring constant of the cantilever. The corresponding depth of penetration is obtained by

$$h = Zp - Zp_0 - Zc, \tag{3}$$

where h is the total penetration depth with respect to the initial contact point, which includes both a recoverable elastic deformation and a permanent plastic deformation, and Zp is the position of the piezoscanner during upward displacement from the contact point made at Zp_0. The system voltage/deflection sensitivity S consists in

$$S = \frac{\Delta Vpd}{\Delta Zc}, \tag{4}$$

which is generally obtained by pressing the tip against a hard reference material such as diamond [6], while collecting the (Zp, Vpd) response, and by assuming that the penetration of the tip during calibration is negligible with respect to Zc, i.e.,

$$h \approx 0 \rightarrow Zc \approx Zp - Zp_0. \tag{5}$$

Two main sources of uncertainty in the standard protocol for measuring hardness in hard substrates using AFM nanoindentation are described in the following. First, it is required to proceed with the determination of k in Eq. (2). A large number of studies have addressed this issue in the past, and have suggested different techniques producing more or less uncertainty in the calculation of this parameter (we refer to Clifford and Seah [28] for a recent overview on this topic). In general, direct FEA approaches give good results with less uncertainty of method, typically below 10% [29], when the probe has an unconventional shape as in the present study. Second, systematic uncertainty in the determination of the sensitivity S in Eq. (4) exists, primarily for two reasons: (i) Silva and Van Vliet [30] invoked the non-linearity of the photodetector voltage–deflection relationship, which may emanate from applying large cantilever deflections [31], and (ii) the assumption of zero indentation into a reference film in Eq. (5) is not satisfied, which is likely the case for stiff AFM cantilevers with $k > 20$ N/m, even if the tip-surface interaction only involves purely elastic deformation during calibration. Furthermore, different methods have been proposed to determine the projected area of contact in hardness measurements by AFM nanoindentation, which varies from directly scanning the residual indent [1,3,4,6,7,10,26] to taking the indenter cross-sectional area into account [3,9]; however, no consensus exists in the literature on the measurement approach resulting in the smallest error.

The objective of this study is to advance the methodology for force calibration and hardness measurements with AFM nanoindentation with a particular focus on nanoindentation with specialty cube-corner diamond tips mounted on AFM sapphire cantilevers with high spring constant (i.e., > 100 N/m). For that purpose, fused quartz, Si(1 0 0) and a 100 nm-thick film of gold deposited on a Si(1 0 0) wafer are used as model materials to verify experimentally the proposed approach. Validation is also performed by comparison with computer simulations using non-linear finite element analysis (FEA).

2. New force-matching calibration method

2.1. Theoretical analysis

The standard calibration becomes statically indeterminate if h is regarded as a non-linear function of Zp, because Zc turns out to be an unknown function of Zp–Zp_0 in Eq. (5) in this case. This issue can be solved if one knows *a priori* the force–depth relationship corresponding to the indentation of a reference material by a tip with same area function than that of the actual tip. For that purpose, we consider the case of a conical indenter with finite tip radius, for which the force–depth relationship takes a quadratic form such as [32]

$$F_i = c_2 h^2 + c_1 h \quad \text{with} \quad h > 0, \tag{6}$$

where F_i is the normal force at depth h and c_i are fitting parameters. Eq. (6) can be determined numerically using the FEA procedure shown below. To accomplish the force calibration, we propose in the following to use a force-matching method. This approach is rooted from atomistic theory where one tries to match as closely as possible the first principles forces from ab-initio calculations on known atomic systems, with those obtained from an interatomic potential in order to model the most accurate constitutive response. By way of analogy, we propose here to match the forces obtained at each data point of the calibration process to "ab-initio" forces F_i on a reference material such as

$$F = F_i. \tag{7}$$

Substituting Eqs. (2) and (6) into Eq. (7) gives

$$Zc \times k = c_2 h^2 + c_1 h \tag{8}$$

Furthermore, it is possible to rearrange Eq. (8) with Eq. (3) as a function of the variable Zc only as follows:

$$AZc^2 + BZc + C = 0 \tag{9}$$

with

$$A = c_2, \tag{10}$$

$$B = -[2c_2(Zp - Zp_0) + c_1 + k], \tag{11}$$

$$C = c_2(Zp - Zp_0)^2 + c_1(Zp - Zp_0). \tag{12}$$

The only root of Eq. (9) to be physically meaningful is found to be

$$Zc = \frac{-B - \sqrt{B^2 - 4AC}}{2A}. \tag{13}$$

By using a reference material such as fused quartz, which exhibits isotropic elastic behavior and hardness essentially

independent of the penetration depth [33], the force-matching method allows us to calculate Zc for each (Zp, Vpd) response using (10)–(13), and to fit a third-order polynomial as suggested by Silva and Van Vliet [30]

$$Zc = a_1(Vpd - Vpd_0)^3 + a_2(Vpd - Vpd_0)^2 + a_3(Vpd - Vpd_0) + a_4, \quad (14)$$

where a_i are fitting parameters with $a_4 \sim 0$. In later experiments, Eq. (14) can be used instead of Eq. (4) to directly compute Zc as a function of Vpd.

2.2. Proposed protocol

With the above analysis, we can propose the following calibration protocol, which takes into account both the tip geometry and the tip-substrate deformation during calibration. It is assumed that the cantilever spring constant k is already known.

Calibration inputs:

(i) Use a calibration grating with sharp inverted tips, such as TGT1 Si gratings (NT-MDT, USA), to obtain a 3D AFM image of the diamond tip. Determine the radius of curvature R at the tip apex and the face angle θ of the pyramidal tip. Calculate the semi-angle α for an equivalent conical indenter using the relation [32]

$$\tan^2(\alpha) = \frac{3\sqrt{3}}{\pi}\tan^2(\theta). \quad (15)$$

(ii) Perform a 2D axisymmetric FEA simulation of indentation into fused quartz with a perfectly-rigid conical indenter with spherical tip. We refer to the work of Yu et al. [27] for more details on the FEA simulation procedure. Predict the force–displacement curve from FEA, and determine the fitting parameters c_1 and c_2 in Eq. (6).

AFM calibration on fused quartz:

(iii) Perform a nanoindentation on fused quartz by displacing the piezoscanner until the maximum voltage measured exceeds that to be used in subsequent experiments. Save the corresponding Zp versus Vpd response into a two-column text file. Determine Zp_0 and Vpd_0 at the point of contact.

(iv) Calculate the cantilever deflection Zc using Eq. (13) for each data point.

(v) Fit a third-order polynomial to Zc as a function of $Vpd–Vpd_0$ to determine the coefficients a_i in Eq. (14).

A computer program in the MATLAB language is provided as Supplementary Data to automate the calculation of the calibration coefficients a_i. The inputs consist of the cantilever spring constant k, the parameter c_1 and c_2 determined in step (ii) and the two-column text file containing raw (Zp, Vpd) data collected in step (iii). Subsequently, the AFM nanoindentation experiment on a specimen with unknown properties can be carried out as follows:

Application of calibration protocol:

(vi) Withdraw the tip from the surface and exchange the fused quartz specimen for the unknown one. In this process, it is imperative that the laser beam alignment and probe position in the holder remain strictly unchanged.

(vii) Scan the specimen in non-contact mode to help positioning the tip onto specific locations of interest.

(viii) Acquire the experimental Zp versus Vpd response. Determine Zp_0 and Vpd_0 at the initial contact point. Calculate Zc and h using Eq. (14) and Eq. (3), respectively. Calculate the applied force F using Eq. (2).

3. Experimental details

AFM nanoindentation experiments were carried out using a universal scanning probe microscope (Quesant, Santa Cruz, CA). A close-loop metrology scanner with three-dimensional capacitive displacement sensors was added to the system in order to improve the spatial resolution in sample positioning. Following the manufacturer's calibration procedure, positioning precisions of 6.5, 9.6 and 0.1 nm were measured along the X, Y and Z

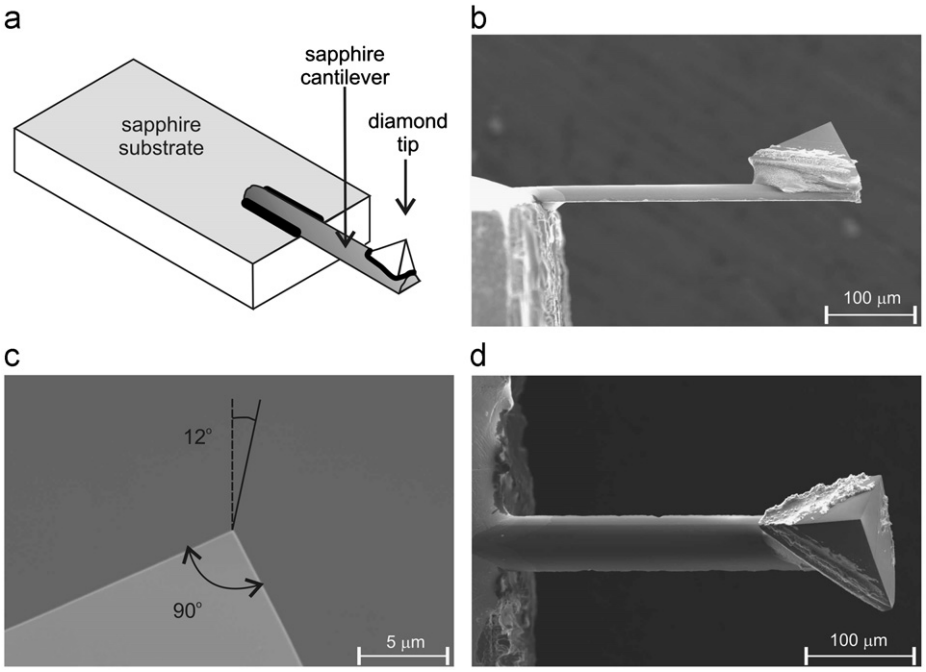

Fig. 2. SEM images of a specialty AFM sapphire cantilever with a cube-corner diamond tip. (a) Schematics of the AFM probe. (b) Side view. (c) Close-up view on the cube-corner tip. (d) Top view.

Table 1
Density and bulk mechanical properties for materials simulated by finite element modeling.

Materials	Density (kg/m^3)	ν	E (GPa)	σ_y (GPa)	E/σ_y
Diamond (tip)	3360	0.07	1150	–	–
Sapphire (AFM cantilever)	3970	0.29	378.7	–	–
Fused quartz	2200	0.17	67.6	5.0	13.52
Si(1 0 0)	2330	0.28[a]	178.6	4.2	42.52
Au	19,320	0.42	89.4	0.8	111.75

[a] Ref. [40]

directions, respectively, for a maximum XY scan size of $40 \times 40\ \mu m^2$ and a vertical Z range of 6.11 μm. A sapphire AFM cantilever with a specifically-designed cube-corner, single-crystal diamond tip (both the cantilever and the tip were assembled by Micro Star Technologies, Huntsville, TX) as shown in Fig. 2, was used to perform both AFM imaging and nanoindentation on flat substrates. The dimensions of the probe were obtained by scanning electron microscopy (SEM) analysis. The face angle of the tip and the radius of curvature at the tip apex were obtained by scanning the probe over a TGT1 Si grating made of 750-nm-high inverted Si tips, and by analyzing the resulting image with the tip detection feature in the software SPIP.

AFM nanoindentations were made on three types of substrate: fused quartz, a phosphorus-doped Si(1 0 0) wafer polished on one side and a gold film of 100 nm in thickness sputtered on a Si(1 0 0) wafer. As shown in Table 1, these substrates have very different elastic–plastic behavior in terms of the ratio E/σ_y where E is the Young's modulus and σ_y is the tensile yield stress. The rate of loading and unloading was varied by changing the speed of Z-displacement of the piezoscanner from 2 to 59 nm s^{-1}. However, no significant creep effects on the nanoindentation curves were detected in each material studied. $2 \times 2\ \mu m^2$ AFM scans with 300 scan lines were conducted in non-contact mode at a frequency of 1 Hz. The shape of each residual impression was determined from these scans by measuring the area of the indent as a function of penetration depth using the threshold detection method in SPIP.

4. Finite element modeling

4.1. Cantilever spring constant

The normal spring constant of the AFM cantilever was determined by linear elastic FEA. This procedure was divided in two steps. First, the exact E value in the sapphire cantilever was determined by predicting the first modal resonant frequency of the cantilever without the probe with an initial value for E equal to 400 GPa, and the material properties shown in Table 1. The resulting frequency was compared with that from the manufacturer obtained before attaching the tip to the cantilever (233 kHz). The elastic modulus of the cantilever was then changed and the process was iterated until the frequency values matched. A 3D solid mesh of the cantilever without the diamond probe was created with ~7000 elements using the dimensions found by SEM analysis. The FFEPlus solver option of the COSMOSWorks FEA software was used to perform the frequency analysis of the sapphire cantilever with a fixed boundary condition at one end. The resonant frequencies were found to match when E equal to 378.7 GPa, which is in good agreement with the value of 403 GPa provided in the literature for sapphire [34].

Second, with the material properties in place, a high quality mesh consisting of ~20,000 elements was used to model the entire probe by FEA. A gradual variance in element size from 0.008 μm at the tip apex to 8.0 μm on the cantilever was imposed due to the large difference in size between the body of the cantilever and the tip. A fixed boundary condition was applied to the end of the cantilever, and a force was applied to the tip with a 12° inclination from the normal of the cantilever face (to account for mounting in the AFM) as shown in Fig. 3. Static deflection of the probe was calculated in the elastic range for a series of forces from 1.0 to 10 μN. We used COSMOSWorks's FFEPlus solver with the large displacement option to predict the stiffness of the probe under bending. The cantilever spring constant calculated from the slope of the force–deflection response was found equal to $k = 906.4$ N/m. This value is significantly higher than the manufacturer's value of 607 N/m, which reveals a systematic error of 50%. A possible reason for this discrepancy is that, in the method used by the manufacturer, both F and Zc are considered at the end of the cantilever beam without accounting for the actual position of the tip. Another reason is due to the fact that in the manufacturer's method F is applied normal to the face of the cantilever with no consideration for the 12° inclination angle of the probe in use in the AFM.

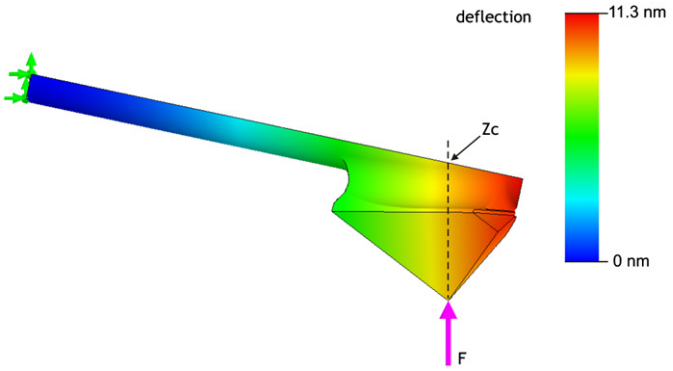

Fig. 3. 3D FEA simulation of elastic deformation in the diamond-tipped AFM cantilever shown in Fig. 2 for an external load $F = 10$ μN.

4.2. Reference nanoindentation response in fused quartz

In order to establish the reference curve in Eq. (6), contact forces as a function of penetration depth were predicted in fused quartz by non-linear static FEA using a 2D axisymmetric nanoindentation model of a perfectly-rigid conical indenter with spherical tip. To this end, we have followed the FEA procedure proposed by Yu et al. [27]. A 3D view of the diamond tip as obtained by scanning the tip on the TGT1 grating is shown in Fig. 4a. The half angle of the equivalent cone and the tip radius measured from this image were found to be equal to $\alpha = 44.37°$ and $R = 74.5$ nm, respectively. A substrate of 2.5 μm in thickness was meshed with less than 1000 elements with greater mesh refinement in the contact zone; a close-up view of the mesh is shown in the inset of Fig. 5. Fixed boundary conditions were applied to the bottom of the mesh. For this simulation, fused quartz was modeled as an elastic-perfectly plastic solid with the properties described in Table 1. It should be noted that according to Yu et al., the elastic modulus for fused quartz and the reduced elastic modulus for the indentation of this material by a diamond tip are 72 GPa and 69.6 GPa, respectively; but for FEA, since the diamond indenter was considered as a rigid body, the elastic modulus of the substrate was chosen equal to 67.6 GPa for consistency [27]. A coefficient of friction of 0.2 was assumed between the tip and the substrate as proposed in Ref. [27]. The tip was displaced by increments of 0.5 nm. The total contact force in the vertical direction and the projected contact area A_c were computed after each increment of displacement.

The evolution of A_c as a function of the contact depth h_c (Fig. 1) as predicted by this FEA simulation is shown in Fig. 4b. This figure

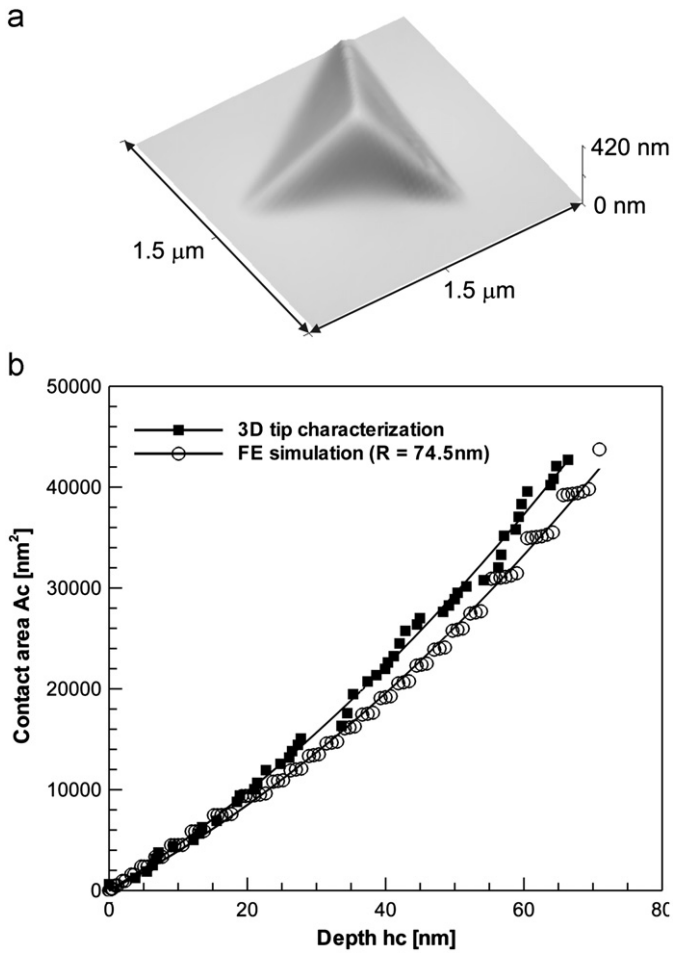

Fig. 4. 3D tip characterization. (a) Reverse image obtained by scanning the diamond tip over a calibration grating TGT1 with an array of sharp, inverted Si tips. (b) Projected contact area as a function of distance from tip apex *hc* calculated from the image in (a) or 2D axisymmetric FEA simulation of conical nanoindentation in fused quartz with a half angle equal to 44.37° and a spherical tip of 74.5 nm in radius.

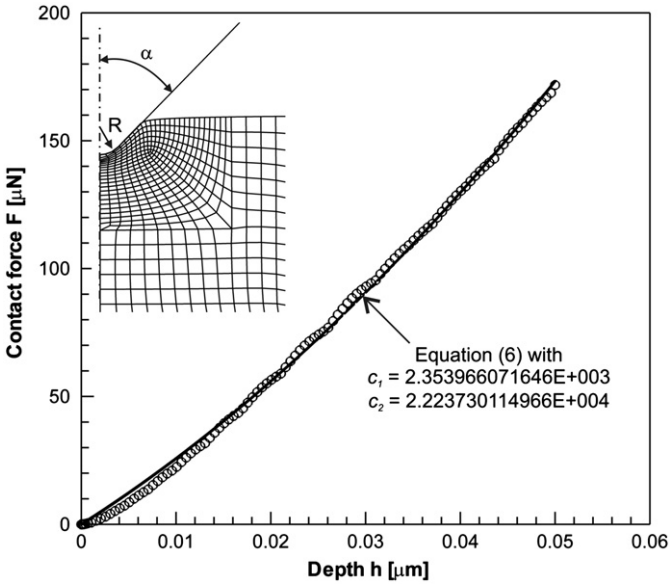

Fig. 5. Force–depth nanoindentation curve on fused quartz (symbols) calculated by a 2D axisymmetric FEA simulation using a rigid conical indenter with spherical tip. The half angle of the cone α is 44.37° and the tip radius R is 74.5 nm, which corresponds to the experimental tip shown in Fig. 4(a). The line represents the fitting of FEA results using (6).

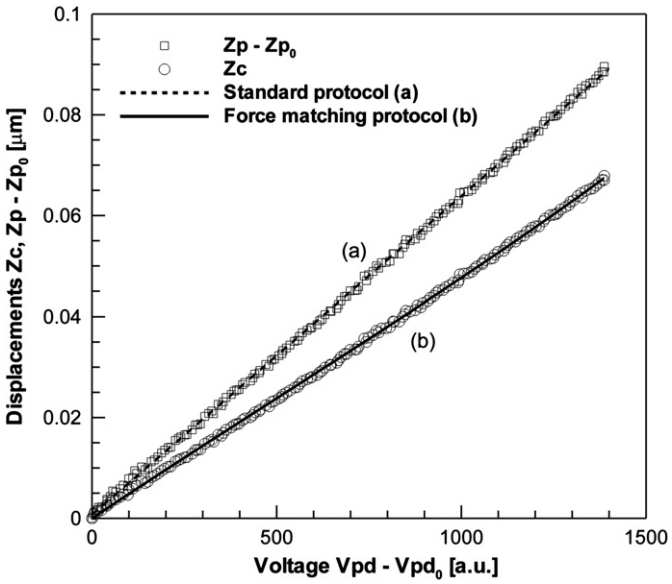

Fig. 6. Results of different calibration protocols on fused quartz. (a) *Zp–Vpd* linear relationship from standard protocol using Eq. (5). (b) *Zc–Vpd* non-linear relationship from force-matching calibration method Eq. (13).

shows that the contact area function agrees very well between FEA simulation and 3D tip characterization, which confirms the validity of the 2D FEA approach used in the present study. The corresponding force–depth relationship predicted by FEA for fused quartz indented by this particular probe is presented in Fig. 5. It is also shown in this figure that the fitting of FEA results with Eq. (6) is excellent for penetration depths up to 40 nm.

In the following, we will also present FEA simulations for different types of substrate, i.e., Si(1 0 0) and Au/Si(1 0 0) using the conical nanoindentation model described herein with the material properties in Table 1. For simplicity, we assumed that all substrates possess an elastic-perfectly plastic behavior.

5. Results and discussion

5.1. Fused quartz

The results of calibration on fused quartz obtained using the standard protocol, as described in Section 1, and the force-matching method are compared in Fig. 6, where the cantilever deflection *Zc* was calculated by using (5) and (13), respectively. This figure shows that the assumption of zero indentation made in the standard approach can significantly overestimate the determination of *Zc* as a function of the measured voltage $Vpd–Vpd_0$. For example, the actual *Zc* value is found to be smaller by 34% in comparison to $Zp–Zp_0$ for a penetration depth of 22.6 nm. It is also important to note that a small degree of non-linearity exists in the *Zc–Vpd* calibration relationship, which is not properly taken into account with the standard calibration method.

We performed a test on fused quartz substrate with a hold time of 10 s imposed at peak force, which revealed that the resulting force–depth response as a function of time (not shown here) showed no significant relaxation effects on the force during the hold time from the AFM system. Also, the applied force was found to increase and decrease linearly, as a function of time, during the loading and unloading portions of the curve,

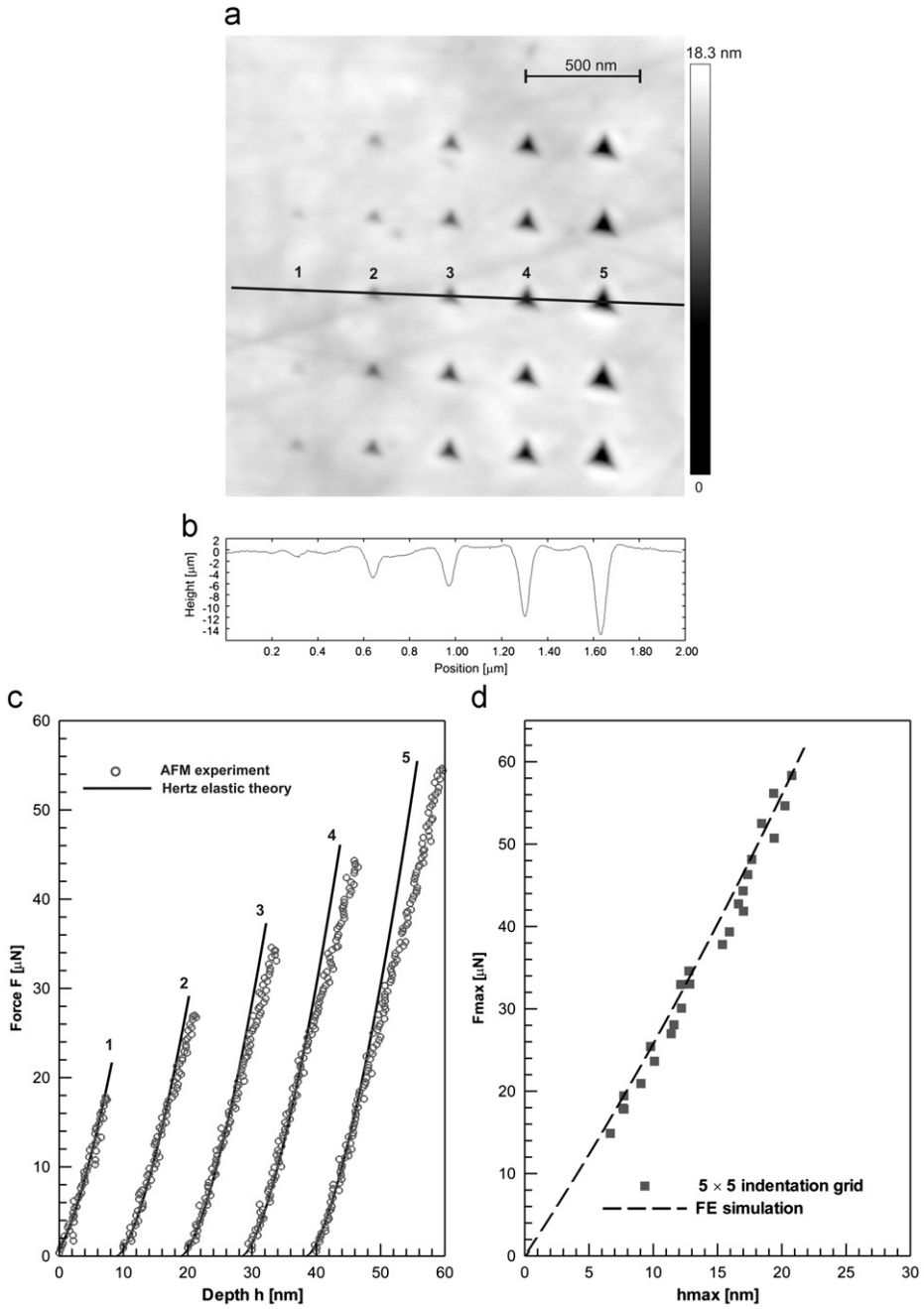

Fig. 7. Matrix of 5 × 5 AFM nanoindentations on fused quartz obtained with constant piezo displacement rate and maximum forces increasing from 14.9 to 58.6 μN (from the upper-left indentation to the lower-right one, respectively). (a) Non-contact AFM image of nanoindentations. (b) Height profile and (c) force–depth nanoindentation curves corresponding to nanoindentations 1–5. Comparison of hertzian elastic theory with AFM experimental data shows excellent agreement at the start of indentation curves. (d) Comparison of maximum applied force between direct AFM measurements and FEA simulations as a function of penetration depth.

Table 2
Mean hardness values measured using matrices of 3 × 3 nanoindentations and reference data reported in the literature.

Materials	AFM Surface Analysis		Force-matching method		Standard method		Reference *H* (GPa)
	h_c (nm)	A_c (nm^2)	F_{max} (μN)	H (GPa)	F_{max} (μN)	H (GPa)	
Fused quartz	11.8 ± 0.9	5041 ± 462	42.4 ± 0.7	8.5 ± 0.8	57.4 ± 0.8	11.5 ± 1.0	8.4[a]
Si(1 0 0)	7.3 ± 0.7	3271 ± 340	57.7 ± 0.6	17.8 ± 1.8	74.4 ± 0.7	23.0 ± 2.3	13.2 – 23.2[b]
Au film on Si(1 0 0)	19.2 ± 3.3	9558 ± 1886	20.8 ± 0.3	2.3 ± 0.4	29.1 ± 0.4	3.2 ± 0.6	2.2 – 3.0[c,d,e]

[a] Ref. [41]; cube-corner tip.
[b] Ref. [5] for 1 nm < h < 12 nm.
[c] Ref. [42]; Berkovich tip.
[d] Ref. [9].
[e] Ref. [26].

respectively. The resolution in force F and penetration depth h measured from the 10-s plateau at peak load was found less than 0.27 μN and 0.77 nm, respectively, which suggests that we have achieved a resolution from our proposed methodology that is at least comparable to that reported with traditional nanoindentation systems [35].

The force-matching calibration protocol was applied to a matrix of 5×5 indentations performed in fused quartz where each indentation was made with a maximum force increasing from 14.9 to 58.6 μN. An AFM topographical image of this indentation matrix is shown in Fig. 7a. The height profile of the line of indentations marked as 1–5 in Fig. 7b shows qualitatively that these impressions vary from purely elastic (e.g., indent 1) to plastic with a residual depth less than 15 nm (e.g., indent 5). More quantitatively, we compare in Fig. 7c the force–depth curves produced on nanoindentations 1–5 with theoretical predictions made using the Hertz elastic theory [36] assuming a spherical tip with $R=74.5$ nm and a reduced elastic modulus of 69.6 GPa for fused quartz. This figure shows that AFM nanoindentation results and the Hertz theory are in excellent agreement in the elastic regime at the start of the curves, which further validates the proposed methodology. Also, Fig. 7c clearly shows the transition from elastic deformation to plastic deformation as the applied force increases. Furthermore, a good agreement between FEA simulation and AFM nanoindentation is shown in Fig. 7d, which represents the evolution of the maximum force as a function of penetration depth for the 25 nanoindentations shown in Fig. 7a.

5.2. Si(100) and Au film on Si(100)

Matrices of 3×3 nanoindentations were carried out in fused quartz, Si(1 0 0) and a 100-nm-thick Au film deposited on Si(1 0 0) for comparison. For each matrix, the nanoindentations were produced by applying the same maximum force F_{max}, but this value was changed from one material to another as shown in Table 2. The surface morphology in the vicinity of a representative impression is shown in Fig. 8 for each specimen. The surface structure is found to be smoother in both fused quartz and Si(1 0 0) than in the Au film. It appears that the Au film is nanocrystalline with a grain size on the order of 100 nm, which is based on the size of the islands formed on its surface. The force–depth curves corresponding to the AFM nanoindentation measurements in Fig. 8 are represented in Fig. 9, and compared to the FEA predictions using a conical indenter. When focusing on the loading and unloading portions of the curves in Fig. 9, it is clear that the AFM nanoindentation technique is able to capture the difference in plastic behavior between the three materials. For example, the AFM nanoindentation of Si(1 0 0) and Au/Si(1 0 0) specimens exhibit more significant plastic deformation than fused quartz, which behaves almost elastically. This result is also supported in Fig. 8 by the detection of plastic pile-ups on the edge of the residual impressions in Si(1 0 0) and Au/Si(1 0 0), while no pile up was visible for fused quartz. It can also be noticed that FEA simulation and experimental data deviate in Si(1 0 0) and (Au)/Si(1 0 0) for large penetration depth, which may result from the fact that these materials do not exhibit an elastic-perfectly plastic behavior, as opposed to our assumption in the FEA simulations. However, the goodness of fit in the elastic regime of the nanoindentation curves provides further evidence for the robustness of the proposed calibration protocol.

5.3. Analysis of contact area and hardness measurements

A key feature of the AFM nanoindentation technique lies in its ability to provide quantitative insights into the surface morphology and projected contact area of residual impressions using non-contact AFM topographical imaging. Fig. 10 represents the measurements of projected area of contact as a function of penetration depth for each impression shown in Fig. 8. It should be noted that these measurements were stopped after the measured area exceeded 25,000 nm^2, i.e. when the film surface was reached. Furthermore, this data is compared with the tip area function determined by scanning the diamond tip over a TGT1 Si grating and presented in Fig. 4b. Fig. 10 reveals that the area of the residual impression measured by AFM imaging is systematically

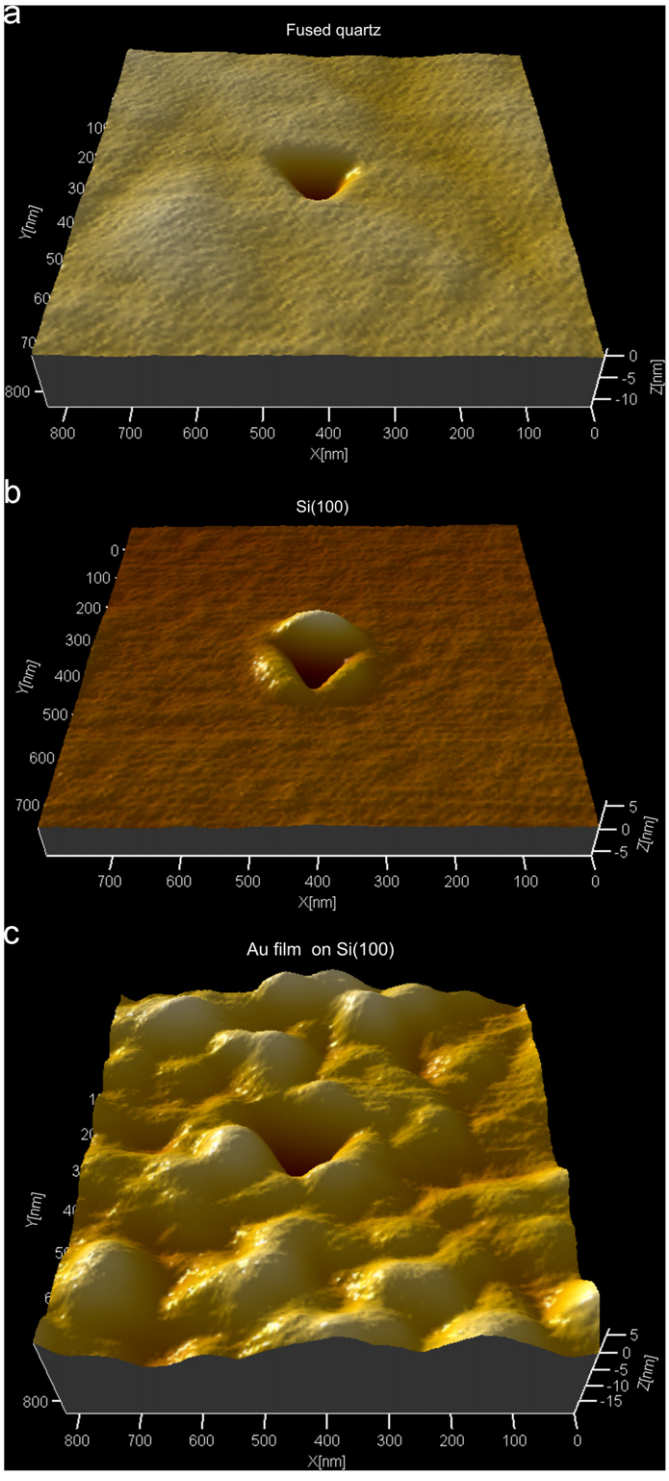

Fig. 8. 1×1 μm^2 topographical AFM image of nanoindentations in (a) fused quartz, (b) Si(1 0 0) wafer and (c) 100-nm-thick film of gold on Si(1 0 0) wafer.

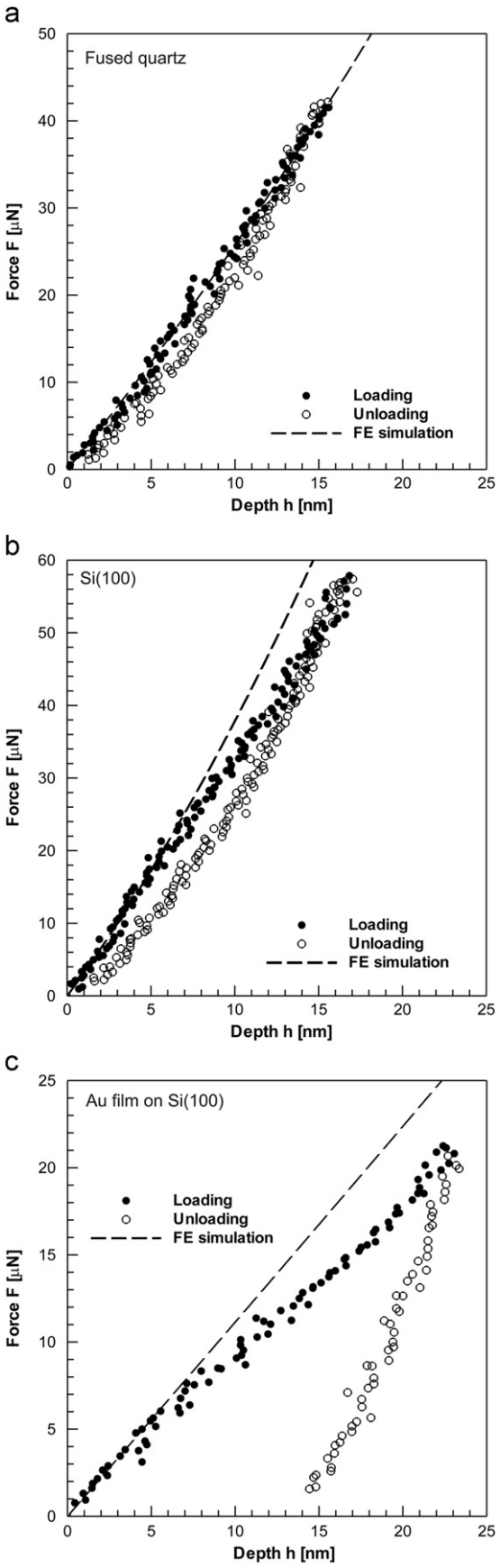

Fig. 9. Force–depth AFM nanoindentation curves corresponding to impressions shown in Fig. 8. Comparison with 2D axisymmetric FEA simulations with model shown in the inset of Fig. 5 and material properties in Table 1.

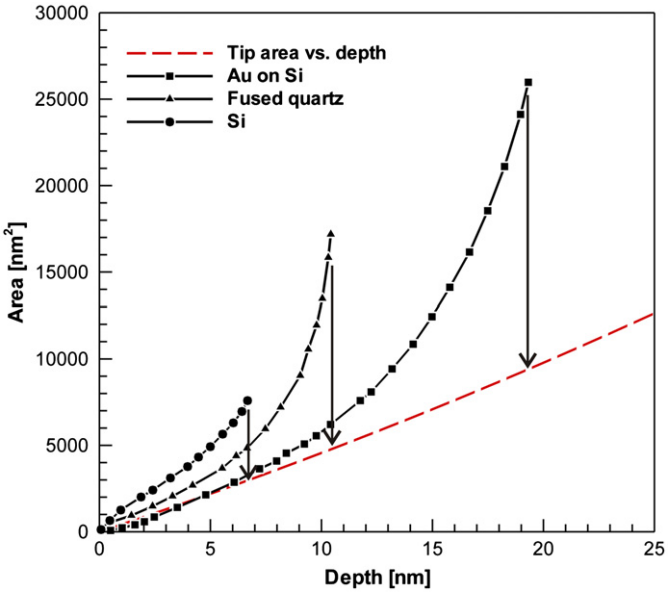

Fig. 10. Direct characterization of projected contact areas as a function of penetration depth using AFM images in Fig. 9. The dash line represents the tip area function fitted in Fig. 4 based on the 3D tip characterization.

larger than the reference area function of the tip for the same depth, regardless of the type of materials. This effect is due to the elastic recovery during withdrawal of the tip, which has first been characterized with an AFM diamond tip by Arnault et al. [37] on Co single crystals, and also by others with different techniques [38,39]. Here, we can interpret the significant elastic recovery in our samples by the fact that the nanoindentations are very shallow (<25 nm in depth). This result therefore suggests that the residual contact area measured directly by AFM scanning is significantly overestimated in comparison to the actual areas during testing. However, a more robust approach to measure hardness from the results in Fig. 10 is to calculate the penetration depth *hc*, assuming that the difference between contact depth and residual depth is negligible for shallow indentations, while the corresponding projected area of contact can be determined using the tip area function presented in Fig. 4.

The projected contact area and hardness values obtained by this method and their averaging over each matrix of nanoindentations are summarized in Table 2. This table shows that the hardness values obtained by AFM nanoindentation measurements with the new force-matching method are in excellent agreement with those reported in the literature for fused quartz, Si(1 0 0) and Au films on Si wafers, while those obtained from the standard method are significantly larger. For example, hardness measurements in fused quartz were found equal to 8.5 ± 0.8 GPa with the force-matching method and 11.5 ± 1.0 GPa with the standard method, which corresponds to systematic errors of 2% and 37%, respectively, in comparison to the reference hardness value of 8.4 GPa [41]. Furthermore, the mean hardness value of 17.8 GPa measured in Si(1 0 0) appears to be in the upper bound of the literature data (i.e., 13.2–23.2 GPa) for this material [5], because the approach used to measure the area of contact in this study did not fully include the pile-up on the edge of the nanoindentations. Therefore the measurements of A_c were likely underestimated for this material.

6. Conclusions

A new AFM protocol based the force-matching method has been proposed to calibrate the application of a force using

diamond-tipped AFM sapphire cantilevers with high spring constant. The novelty of this approach is to take into account the tip-surface deformation during calibration and the actual tip morphology. This study shows that the systematic error obtained by using the standard calibration method to measure the hardness of different substrates, metallic and semiconductors, can be markedly reduced with the new approach. We have verified the proposed calibration method by conducting AFM nanoindentations on flat substrates including fused quartz, Si(1 0 0) substrate and a 100-nm-thick film of gold deposited on Si(1 0 0). The results suggest that AFM nanoindentation technique can achieve resolutions in both force and penetration depth at least comparable to those reported with traditional nanoindentation systems. A key advantage of *in-situ* AFM nanoindentation over other types of system is the ability to quantify the elastic recovery effects when the tip is withdrawn, by non-contact AFM imaging. This approach is shown to notably improve the accuracy in measuring the projected area of contact at maximum force for hardness calculations with extremely shallow nanoindentations. The proposed method is general, and could also be used to study the hardness of low-dimensional nanostructures such as nanowires and nanoparticles, which remained difficult to achieve experimentally.

Acknowledgements

TG acknowledges support from the URECA! and HELiX programs at the University of Vermont. FS acknowledges support from the National Science Foundation CAREER program (Grant DMR-0747658) and the Outwater Funding Award at the University of Vermont. We also thank Evan Malina for performing the AFM imaging of the tip on the TGT1 grating and its characterization using SPIP.

Appendix A. Supplementary materials

Supplementary data associated with this article can be found in the online version at doi:10.1016/j.ultramic.2010.09.012.

References

[1] B. Bhushan, V.N. Koinkar, Nanoindentation hardness measurements using atomic force microscopy, Appl. Phys. Lett 64 (1994) 1653–1655.
[2] A.G. Khurshudova, K. Katob, H. Koide, Wear of the AFM diamond tip sliding against silicon, Wear 203-204 (1997) 22–27.
[3] T. Bao, P.W. Morrison Jr, W. Woyczynski, AFM nanoindentation as a method to determine microhardness of hard thin films, Mat. Res. Soc. Symp. Proc. 517 (1998) 395–400.
[4] K. Pohlmann, B. Bhushan, K.H. Gahr, Effect of thermal oxidation on indentation and scratching of single-crystal silicon carbide on microscale, Wear 237 (2000) 116–128.
[5] E.V. Anoikin, G.S. Ng, M.M. Yang, J.L. Chao, J. Elings, D. Brown, Ultrathin protective overcoats on magnetic hard disks, IEEE Trans. Magn. 34 (1998) 1717–1719.
[6] S. Garcia-Manyes, A.G. Guell, P. Gorostiza, F. Sanz, Nanomechanics of silicon surfaces with atomic force microscopy: an insight to the first stages of plastic deformation, J. Chem. Phys. 123 (2005) 114711.
[7] S. Graca, R. Colaço, R. Vilar, Using atomic force microscopy to retrieve nanomechanical surface properties of materials, Mater. Sci. Forum 514-516 (2006) 1598–1602.
[8] K. Degiampietro, R. Colaço, Nanoabrasive wear induced by an AFM diamond tip on stainless steel, Wear 263 (2007) 1579–1584.
[9] Y.D. Yan, T. Sun, S. Dong, Study on effects of tip geometry on AFM nanoscratching tests, Wear 262 (2007) 477–483.
[10] M. Lucas, K. Gall, E. Riedo, Tip size effects on atomic force microscopy nanoindentation of a gold single crystal, J. Appl. Phys. 104 (2008) 113515.
[11] M. Alderighi, V. Ierardi, F. Fuso, M. Allegrini, R. Solaro, Size effects in nanoindentation of hard and soft surfaces, Nanotechnology 20 (2009) 235703.
[12] M.R. VanLandingham, J.S. Villarrubia, W.F. Guthrie, G.F. Meyers, Recent progress in nanoscale indentation of polymers using the AFM, in: Proceedings of the SEM IX International Congress on Experimental Mechanics, 2000, pp. 912–915.
[13] B. Du, J. Zhang, Q. Zhang, D. Yang, T. He, Nanostructure and mechanical measurement of highly oriented lamellae of melt-drawn HDPE by scanning probe microscopy, Macromolecules 33 (2000) 7521–7528.
[14] F. Bedoui, F. Sansoz, N.S. Murthy, Incidence of nanoscale heterogeneity on the nanoindentation of a semicrystalline polymer: experiments and Modeling, Acta Mater. 56 (2008) 2296–2306.
[15] B. Mesa, S. Magonov, Novel diamond/sapphire probes for scanning probe microscopy applications, J. Phys: Conf. Ser. 61 (2007) 770–774.
[16] X. Li, H. Gao, C.J. Murphy, K.K. Caswell, Nanoindentation of silver nanowires, Nano Lett. 3 (2003) 1495–1498.
[17] S. Bansal, E. Toimil-Molares, A. Saxena, R.R. Tummala, Nanoindentation of single crystal and polycrystalline copper nanowires, Elec. Comp. Tech. Conf. 1 (2005) 71–76.
[18] G. Feng, W.D. Nix, Y. Yoon, C.J. Lee, A study of the mechanical properties of nanowires using nanoindentation, J. Appl. Phys. 99 (2006) 074304.
[19] X. Tao, X. Li, Catalyst-free synthesis, structural, and mechanical characterization of twinned Mg2B2O5 nanowires, Nano Lett. 8 (2008) 505–510.
[20] T.H. Fang, W.J. Chang, Nanolithography and nanoindentation of tantalum-oxide nanowires and nanodots using scanning probe microscopy, Physica B 352 (2004) 190–199.
[21] G. Stan, C.V. Ciobanu, P.M. Parthangal, R.F. Cook, Diameter-dependent radial and tangential elastic moduli of ZnO nanowires, Nano Lett. 7 (2007) 3691–3697.
[22] H. Zhang, J. Tang, L. Zhang, B. An, L.C. Qin, Atomic force microscopy measurement of the Young's modulus and hardness of single LaB6 nanowires, Appl. Phys. Lett. 92 (2008) 173121.
[23] M. Lucas, A.M. Leach, M.T. McDowell, S.E. Hunyadi, K. Gall, C.J. Murphy, E. Riedo, Plastic deformation of pentagonal silver nanowires: comparison between AFM nanoindentation and atomistic simulations, Phys. Rev. B 77 (2008) 245420.
[24] D.A. Bonnell, S.V. Kalinin, A.L. Kholkin, A. Gruverman, Piezoresponce force microscopy: a window into electromechanical behavior at the nanoscale, MRS Bull. 34 (2009) 648–657.
[25] R.J. Emerson, T.A. Camesano, On the importance of precise calibration techniques for an atomic force microscope, Ultramicroscopy 106 (2006) 413–422.
[26] B. Kracke, B. Damaschke, Measurement of nanohardness and nanoelasticity of thin gold films with scanning force microscopy, Appl. Phys. Lett. 77 (2000) 361–363.
[27] N. Yu, A.A. Polycarpou, T.F. Conry, Tip-radius effect in finite element modeling of sub-50 nm shallow nanoindentation, Thin Solid Films 450 (2004) 295–303.
[28] C.A. Clifford, M.P. Seah, The determination of atomic force microscope cantilever spring constants via dimensional methods for nanomechanical analysis, Nanotechnology 16 (2005) 1666–1680.
[29] J.M. Neumeister, W.A. Ducker, Lateral, normal, and longitudinal spring constants of atomic force microscopy cantilevers, Rev. Sci. Instrum. 65 (1994) 2527.
[30] E.C.C.M. Silva, K.J. Van Vliet, Robust approach to maximize the range and accuracy of force application in atomic force microscopes with nonlinear position-sensitive detectors, Nanotechnology 17 (2006) 5525–5530.
[31] L.Y. Beaulieu, M. Godin, O. Laroche, V. Tabard-Cossa, P. Grutter, A complete analysis of the laser beam deflection systems used in cantilever-based systems, Ultramicroscopy 107 (2007) 422–430.
[32] A.C. Fisher-Cripps, Nanoindentation, second ed., Springer, New York, 2004.
[33] W.D. Nix, H. Gao, Indentation size effects in crystalline materials: a law for strain gradient plasticity, J. Mech. Phys. Solids 46 (1998) 411–425.
[34] G. Simmons, H. Wang, Single crystal elastic constants and calculated aggregate properties: a handbook, second ed., MIT Press, Cambridge, 1971.
[35] W.C. Oliver, G.M. Pharr, Measurement of hardness and elastic modulus by instrumented indentation: advances in understanding and refinements to methodology, J. Mater. Res. 19 (2004) 3–20.
[36] K.L. Johnson, Contact Mechanics, Cambridge University Press, Cambridge, 2004.
[37] J.C. Arnault, A. Mosser, M. Zamfirescu, H. Pelletier, Elastic recovery measurements performed by atomic force microscopy and standard nanoindentation on a Co(10.1) monocrystal, J. Mater. Res. 17 (2002) 1258–1265.
[38] D. Tranchida, S. Piccarolo, M. Soliman, Nanoscale mechanical characterization of polymers by AFM nanoindentations: critical approach to the elastic characterization, Macromolecules 39 (2006) 4547–4556.
[39] J.H. Strader, S. Shim, H. Bei, W.C. Oliver, G.M. Pharr, An experimental evaluation of the constant β relating the contact stiffness to the contact area in nanoindentation, Phil. Mag. 86 (2006) 5285–5298.
[40] W.A. Brantley, Calculated elastic constants for stress problems associated with semiconductor devices, J. Appl. Phys. 44 (1973) 534–535.
[41] T. Chudoba, P. Schwaller, R. Rabe, J.M. Breguet, J. Michler, Comparison of nanoindentation results obtained with Berkovich and cube-corner indenters, Phil. Mag. 86 (2006) 5265–5283.
[42] E.T. Lilleodden, W.D. Nix, Microstructural length-scale effects in the nanoindentation behavior of thin gold films, Acta Mater. 54 (2006) 1583–1593.